



CHORUS

This is the accepted manuscript made available via CHORUS. The article has been published as:

Programmable ion-sensitive transistor interfaces. I. Electrochemical gating

Krishna Jayant, Kshitij Auluck, Mary Funke, Sharlin Anwar, Joshua B. Phelps, Philip H. Gordon, Shantanu R. Rajwade, and Edwin C. Kan

Phys. Rev. E **88**, 012801 — Published 1 July 2013

DOI: [10.1103/PhysRevE.88.012801](https://doi.org/10.1103/PhysRevE.88.012801)

Programmable Ion Sensitive Transistor Interfaces

I. Electrochemical Gating

Krishna Jayant ^{¶}, Kshitij Auluck[¶], Mary Funke ^{‡¶}, Sharlin Anwar ^{£¶}, Joshua B. Phelps[¶],*

Philip H. Gordon[¶], Shantanu R. Rajwade[¶] and Edwin C. Kan[¶]

[¶]Electrical and Computer Engineering, Cornell University, Ithaca, NY 14853, USA

[‡]Department of Chemistry, High Point University, NC 27262, USA

[£]Department of Biomedical Engineering, City College New York, NY 10031, USA

[¶]Equal Contribution

Corresponding Email Address* :

*Krishna Jayant (kj75@cornell.edu)

School of Electrical and Computer Engineering, Cornell University Ithaca, NY 14853 USA
(phone: 908-930-7179)

(Received Date- February 26th, 2013)

PACS number(s): 73.40.Mr, 82.47.Rs, 68.47.Pe, 87.80.-y, 85.30.Tv, 87.85.Ox

ABSTRACT

Electrochemical gating is the process in which an electric field normal to the insulator electrolyte interface shifts the surface chemical equilibrium and further affects the charge in solution [Z. Jiang, and D. Stein, Langmuir 26, (2010)]. The surface chemical reactivity and double-layer charging at the interface of electrolyte-oxide-semiconductor (EOS) capacitors is first investigated. We find a strong pH-dependent hysteresis upon DC potential cycling. Varying salinity at a constant pH did not change the hysteretic window, implying that field-induced surface pH regulation is the dominant cause of hysteresis. We then propose and investigate this mechanism in foundry-made floating-gate ion-sensitive field-effect transistors (ISFET's), which can serve both as an ionic sensor and actuator. Termed as the chemoreceptive neuron MOS transistor (CvMOS), it features independently-driven control (CG) and sensing gates (SG) that are capacitively coupled to an extended floating gate (FG). The SG is exposed to fluid, CG is independently driven and the FG is capable of storing charge (Q_{FG}) of either polarity. Asymmetric capacitive coupling between the CG/SG to FG results in intrinsic amplification of the measured surface potential shifts, and influences the FG charge injection mechanism. This modified SG surface condition was monitored through transient recordings of the output current, performed under alternate positive and negative CG pulses. Transient recordings revealed a hysteresis where the current was enhanced under negative pulsing and reduced after positive pulsing. This hysteresis effect is similar to that observed with EOS capacitors suggesting a field dependent surface charge regulation mechanism at play. At high CG biases, non-volatile charge (Q_{FG}) tunneling into the FG occurs, which creates a larger field and tunes the pH response and the point of zero charge. This mechanism gives rise to *surface programmability*. In part I, we describe the operational principles, tunneling mechanism, and the role of electrolyte composition

under field modulation. The experimental findings are then modeled by a Poisson Boltzmann (PB) formulation with surface pH regulation. We find that surface ionization constants play a dominant role in determining the pH tuning effect. In part II, we extend the dual-gate operation to molecular sensing, and demonstrate the use of Q_{FG} to achieve manipulation of surface-adsorbed DNA.

I. INTRODUCTION

Transistor-based biological/chemical transducers have gained considerable attention over the last decade [1-3]. The Ion Sensitive Field Effect Transistor (ISFET) [2] has its gate oxide directly exposed to the electrolyte with its electrochemical potential set by a solution reference electrode. The oxide interface possesses a net surface charge due to hydroxyl groups upon exposure to the electrolyte. The charge density and the electrostatic potential then decay from the interface into the solution bulk over the characteristic distance of the Debye length. A change in the oxide-electrolyte interface potential due to ionic adsorption or reference-electrode biasing then induces a shift in the channel current via a change in the electric field in the gate oxide. The change in the reference electrode potential with respect to the transistor source bias to achieve a constant channel current (i.e. a constant field in the gate oxide) is thus a direct measure of the oxide-electrolyte interface potential shift [4]. The transistor is typically only sensitive to ionic and molecular charges within a few Debye lengths from the interface. While numerous examples of FET-based ionic and molecular sensors have been demonstrated [3, 5-7], the ability to dissect the complex interplay between pH, salinity and surface chemistry is still unclear. In addition, the ability to impart electrical control over the sensing interface concomitantly is still elusive. Dynamic control of surface charge can potentially realize reversible interfaces [8], addressable sensor pixels in large-scale arrays, controlled charge modulation [9], and even local pH titration [10] with simultaneous detection. However, since ISFET generally has an exposed dielectric interface which consists of amphoteric surface groups, a change in electric field within the oxide would not only modulate ions in solution but also affect the chemical composition of the interface.

Similarly, when an electrode covered by an insulator is biased in an electrolytic medium, the field in the insulator would thereby modulate the ionic double layer [9]. The applied potential to such an electrode or static stored charge on a buried floating electrode can in turn influence the insulator's surface charge according to its amphoteric nature, which then affects the proton binding affinity, the adsorption equilibrium and the net charge in the double layer. The interplay between the applied field and the chemical equilibrium at the interface is termed as "electrochemical gating" [9]. The first examples of electrochemical gating in microfluidic systems by Ghowsi et al. [11] and Schassfoort et al. [12] demonstrated that local fields could modulate the electroosmotic flow in micro-channels, but did not elaborate on the chemical properties of the interface. Karnik et al. [13], Fan et al. [14] and Guan et al. [15] demonstrated field-effect control within fluidic channels, which leads to ionic modulation and subsequent protein transport. Fan and coworkers [14] further highlighted that chemical functionalization strongly affected the ionic polarity within the channel. Several recent examples, including three-terminal control within a fluidic network [16] and electrically gated nanopores [17-21], show similarities to gate modulation of the channel carriers in MOSFET, which can be viewed as fluidic analogues of electronic transistors. Jiang et al. [9, 21] highlighted the effect of surface chemistry on ionic regulation in the electrolyte at an electrically gated dielectric interface. They found that surface charge density and hence protonation and deprotonation impose limits on the nonlinear charging property of the double layer. The pH at the interface was observed to be field-dependent, which further affected ion modulation. This is specifically important in manipulating molecules by Coulombic forces with careful consideration of the hydration and ionic screening effects. Recently McKinnon and colleagues [22] theoretically showed that changing the field in the gate oxide had a profound effect on biomolecular sensitivity primarily due to ionic depletion

at the interface. This implies a possible strategy to implement chemical/bio sensors with an electrically tunable interface to achieve high sensitivity and specificity.

In order to develop an intuitive understanding of our approach, we first consider a conventional electrolyte-oxide-semiconductor (EOS) [Fig. 1(a), Supplemental Material Fig. S1(a)] system, where electrochemical gating modulates the surface charge. AC measurements using capacitive electrode structures are frequently employed to measure the net charge modulation in the electrolyte. However, measuring capacitances on the order of pF to aF in many lab-on-chip (LOC) systems often requires complex circuitry and a long averaging time, and is thus prone to noise. It is much easier to measure charge via transistors at such scales, as the output current can be sampled more easily. If one intentionally introduces a highly conductive slab as a floating gate (FG) [Supplemental Material, Fig. S1(b)] in between the reference electrode and oxide-electrolyte interface, the charge modulation in the electrolyte now depends on the electric field between the FG and electrolyte bulk. The FG potential is determined by the weighted inputs of all capacitors coupled to the FG and additionally the nonvolatile charge it stores. The change in surface charge or ionic charge in the double layer will thus affect the FG potential. The question remains as whether one can measure the FG potential directly to estimate the electrolyte charge. By coupling a transistor capacitively to the FG, the current output is an accurate measure of the FG potential. This transistor concept is termed as the chemoreceptive neuron MOS transistor (CvMOS) [23] [Fig. 1(b), Supplemental Material, Fig. S1(c)].

The CvMOS [23] [Fig. 1(b)] is a multi-gate transistor with control (CG) and sensing gates (SG) coupled to FG. The CG alleviates the sole reliance on biasing from the reference electrode V_{REF} , which is important from a reliability and pixel-level biasing perspective. The reference electrode (Ag/AgCl) can still be used to pin the electrolyte bulk. This scheme has multiple advantages: (i)

suitable fluid biasing can lower the read voltage from the control gate and enlarge the sensing range, (ii) the pinned electrolyte potential results in fast ion settling time, and (iii) the CG can be used in feedback to maintain the optimal signal-to-noise ratio (SNR) condition without changing the reference electrode bias. Due to the possible asymmetric capacitances between the two gates, the voltage measured from the CG to maintain the same channel current can be intrinsically amplified if $C_{CG} < C_{SG}$. At high CG biases, Fowler-Nordheim (FN) tunneling ensues to inject nonvolatile charge onto the FG, which can in turn render a strong field in the SG oxide even after the CG bias is removed. We experimentally investigate the role of electrolyte composition on the transistor characteristic both with and without FG charges and corroborate our measurements against standard (EOS) capacitors with similar chemically reactive interfaces.

II. METHODS

A. Materials

EOS capacitors [Fig. 1(a)] were fabricated on p-type silicon wafers after standard MOS cleaning. About 20nm of thermal SiO₂ was grown, followed by 30nm growth and patterning of LPCVD polysilicon with n⁺ doping. Atomic-layer deposition (ALD) of nitride as a protective coating was then deposited and patterned to expose only the polysilicon gate to solution. The CvMOS transistors were fabricated in a 1.5 μm AMI foundry process as described previously [23]. Briefly, the tunnel oxide refers to the oxide between the channel and the FG, while the control oxides represent the oxide between the CG/SG and FG. The FG is electrically floating and does not have any direct conducting path to the electrolyte or other electrodes. The reference electrode pins the electrolyte bulk to (V_{REF}) while the CG can be pulsed to program or erase the device. The tunnel and control oxide thicknesses are 10nm and 35nm, respectively. The control gate area is 25 μm ×40 μm while sensing gates vary between 5 μm ×400 μm and 200 μm ×400 μm . An

SEM image of the fabricated chip is shown in Fig. 1(c). The chip was cleaned with DI water and isopropyl-alcohol (IPA) before each test. A small reservoir made of epoxy was created to isolate the fluid from the bond pads.

Electrolytes containing $NaCl$, $MgCl_2$ and $Co(NH_3)_6Cl_3$ salts (Sigma Aldrich) were made up to the desired dilution using Millipore de-ionized H_2O . The pH of the solutions was regulated using conjugate acid-base mixtures. TE buffer (10mM TRIS pH 8, 10mM NaCl and 1mM EDTA) was added to test for buffering effects. Electrodes made of $Ag / AgCl$ were used as reference electrodes. Experiments were performed in a light-tight environment.

B. Electrical instrumentation

Capacitance-voltage (CV) measurements were performed using a Keithley 4200 semiconductor parameter analyzer. CV profiles were recorded at various small-signal frequencies. The reference electrode was supplied with an AC signal superimposed on a slow DC sweep, while the wafer chuck was used as ground. The transistor transfer characteristics (the drain current I_D vs. the CG bias (V_{CG})) were recorded using a Keithley 236 source measure unit (SMU) for the drain ($V_D = 1V$) and a Keithley 2400 was used to sweep V_{CG} . Programming was carried out by applying a large positive voltage to V_{CG} with a +1V bias on V_D unless otherwise specified, while erasing was by a large-magnitude negative voltage. The transient measurements at constant V_{CG} were recorded by the trans-impedance amplifier (TIA, Stanford Research Systems SR570, CA, USA) with a sensitivity of $100 \frac{\mu A}{V}$ and low-pass filtering at 3KHz. The data was collected on a computer through a data acquisition test board (NI BNC 2110 and NI USB 6259). The bias on the TIA was set to 1V. Prior to measurements, the transconductance (g_m) seen from both the CG and SG was recorded in order to calibrate the capacitance ratio.

III. DEVICE OPERATION AND SENSING PRINCIPLES

A. Capacitive amplification

The CvMOS sensor works on the principle of the conventional neuron MOS transistor [23, 24] where two input gates are coupled to a common FG. The potential on the FG (V_{FG}) can be calculated by the capacitive divider model shown in Fig. S2 (Supplemental Material). Additionally, a net charge Q can be stored on FG via tunneling. The constant current readout implies that V_{FG} is brought back to the same point. This can be achieved via V_{CG} or V_{REF} . The capacitance ratio between the SG and CG to the FG ($\frac{C_{SG}}{C_{CG}}$) sets the scaling factor. Thus an asymmetric CvMOS structure can lead to a magnification of the threshold voltage shift (Eq. 1) as observed from the control gate when the sensing gate experiences a load from the electrolyte.

$$\Delta V_{th_CG} = \frac{C_{SG}}{C_{CG}} \cdot (\Delta \psi_o) \quad (1)$$

The governing equations are listed in Table S-I (see Supplemental Material). Recent reports [6, 25] have proposed similar concepts and claimed to have beaten the Nernst sensitivity limit of 59mV/pH. We reiterate that this technique merely scales the surface potential shift and does not signify any change in the intrinsic properties [5, 26] of the electrolyte interface. The amplification method does however reduce the burden on supporting circuitry to sense the voltage shift [26]. Theoretically, the capacitive amplification factors should have achieved values between 70~90 for the layouts used in this study. However, due to parasitics we experimentally observed factors of 10~30 [Supplemental Material, Fig. S6(a)].

B. Programming and erase operations

In conventional Flash memory devices when the CG bias is swept to a large magnitude, sufficient electric field can develop across the gate stack enabling electron/hole tunneling from the silicon channel onto the FG (Q_{FG}). “Programming” is the condition when the FG has a net stored charge state, while “erase” is the condition under which that charge is removed (Supplemental Material, Fig. S3). The field in the oxide during tunneling is quite high ($0.8 \sim 1 \frac{V}{nm}$) which is a pre-requisite for Fowler-Nordheim (FN) tunneling. Such fields are quite common in Flash memory devices [27] and can be employed many times without permanent breakdown [28]. The CvMOS has an EOT (effective oxide thickness) of approximately 50nm and the maximum CG bias for programming does not exceed 40V.

The CG is shielded from the solution by a large passivation oxide ($> 2\mu m$) and hence the CG bias has no direct influence on the electrolyte except through the FG and SG coupling. The SG surface is highly-doped polysilicon which is widely being considered for biosensing applications [3, 29, 30]. At high V_{CG} , the electric field in the CG control oxide (E_{CG_OX}) increases. Normally V_{FG} would rise together with V_{CG} . However the FG is coupled to V_{REF} through the large SG which ensures that V_{FG} does not increase much with an increase in V_{CG} . This directly affects E_{CG_OX} as it rises considerably higher than the field in the tunnel oxide (E_{TOX}).

For example, given a capacitvie ratio of 20, a 40V CG bias induces only a $\sim 2V$ rise in V_{FG} . Evidently this would cause a larger change in E_{CG_OX} than in E_{TOX} . Electrons thus tunnel out of the FG onto the CG faster than they tunnel onto the FG from the channel. This causes a net positive stored charge on the FG and lowers the threshold voltage V_{th} . However, if V_{CG} is

large and negative, the opposite occurs resulting in net electron storage. The energy band diagrams depicting this operation are shown in (Supplemental Material, Fig. S3).

If the reference electrode is left floating, the capacitive coupling in the SG branch is much weaker and V_{FG} is then allowed to track V_{CG} . The E-field in this case aids electron injection from the channel into the FG during programming and hole storage during erase [Supplemental Material, Fig.S3 (c&e)], similar to conventional Flash memory operation.

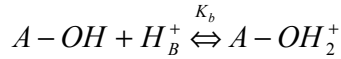
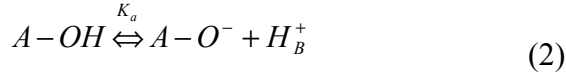
Thus by flipping the reference electrode between floating and biasing conditions during the programming process, the polarity of stored charge on the floating node can be significantly changed. This nonvolatile charge then capacitively interacts with the fluid via the field effect. A simulation of the tunneling effect with and without the reference electrode is shown in Fig. S6(b) (see Supplemental Material). Electrostatics of the system is represented by the capacitors C_{DL} (double layer), C_{SG} (sensing gate), C_{CG} (control gate) and C_{tunnel} (tunnel oxide), respectively. This network is solved self-consistently with a Tsu-Esaki tunneling formulation [31] which is represented by voltage-controlled current sources.

The SG-fluid interface is considered to be in steady state during the program pulse and V_{th} measurement ramp. Dynamic processes of ion or water dipole rearrangement are assumed to occur at time scales much faster than tunneling. The double layer capacitance (C_{DL}) is modeled based on a Poisson-Boltzmann formulation including ion Steric effects [32].

C. Role of surface groups and electrochemical gating

The ISFET or EOS response is generally dictated by the protonation behavior of the interfacial inorganic oxide in direct contact with the electrolyte. Surface hydroxyl groups are amphoteric in nature, protonated or deprotonated depending on the solution bulk pH (pH_B), resulting in a net surface charge σ_o . It is this shift in charge that determines the net pH_B sensitivity of the

underlying transistor. Jiang and Stein [9] theoretically proved that in addition to pH_B , the field in the underlying oxide profoundly affected σ_o , which further influenced the surface pH sensitivity (pH_S). We adopt a hydroxyl surface group model [9, 33] where the basic acid-base equilibrium at the interface is given by Eq. (2).



Here K_a and K_b are the dissociation constants and H_B^+ is the bulk proton concentration. At a particular pH_B , the interface is charge neutral. This is termed as pH_{PZC} , i.e., the pH at the point of zero surface charge. However, when pH_B is not equal to pH_{PZC} , the surface pH (pH_S) shifts in response to the change in pH_B . The number of surface groups that ionize in response to varying pH_S is termed as the buffer capacity (β_S) and its associated capacitance [4] is termed as C_{Buffer} . By definition, β_S is the ratio of the change in net surface charge to that in pH_S .

$$\beta_S = \frac{d[\sigma_o]}{dpH_S} \quad (3)$$

Here σ_o is equal to the net number of titrated groups per area:

$$\sigma_o = -e \cdot \Gamma^{O^-} + e \cdot \Gamma^{OH_2^+} \quad (4)$$

where $N_S = \Gamma^O = \Gamma^{O^-} + \Gamma^{OH_2^+} + \Gamma^{OH}$ is the total number density of ionizable surface groups and is a constant for a given surface depending on the chemical composition and surface functionalization. Using the relationship between $K_a = \frac{H_S^+ \cdot \Gamma^{O^-}}{\Gamma^{OH}}$, $K_b = \frac{H_S^+ \cdot \Gamma^{OH}}{\Gamma^{OH_2^+}}$ and Γ^O , and

under the assumption of a single pK model (i.e. $pK_a = -\log_{10}(K_a)$), i.e., when only one type of surface group of O^- is considered, Eq. (4) can be rewritten as,

$$\sigma_o = \frac{-e \cdot \Gamma^o}{1 + \frac{H_S^+}{K_a}} \quad (5)$$

If we consider both surface ionization reactions i.e., a 2pK site-binding model, Eq. (4) then becomes

$$\sigma_o = e \cdot \Gamma^{OH} \cdot \left(\frac{H_S^+}{K_b} - \frac{K_a}{H_S^+} \right) \quad (6)$$

We can then solve for Γ^{OH} by using the relationship between K_a , K_b and Γ^o .

Here the surface proton activity H_S^+ is related to the bulk proton activity H_B^+ by the Boltzmann relation

$$H_S^+ = H_B^+ \cdot \exp\left(-\frac{e(\psi_o - V_{REF})}{kT}\right) \quad (7)$$

The simulation considers a metal electrode below an insulator exposed to the electrolyte (Metal-oxide-electrolyte) [Fig. 1(a)] similar to the model structure considered by Jiang and Stein [9].

The electrolyte bulk potential (V_{REF}) is held at ground. On applying a potential sweep to the metallic electrode with respect to V_{REF} , two compensating charges at the electrolyte-oxide interface will respond: 1) protonation/deprotonation of the surface hydroxyl groups, denoted by σ_o , and 2) the double layer charge, σ_{DL} (see next section). The field in the oxide is then given

by

$$E_{OX} = \frac{-[\sigma_o + \sigma_{DL}]}{\epsilon_{OX}} \quad (8)$$

Equation (8) is then solved self consistently for the entire electrostatic system.

D. Electrical double layer charge (σ_{DL})

The SG-electrolyte interface is commonly described by the Gouy-Chapman-Stern (GCS) model which considers ions as point charges. When a solid interface is exposed to electrolyte, ionization or ion adsorption creates a net surface charge density σ_o . This results in a strong attraction of counterions towards the interface to neutralize the immobile surface charge denoted by σ_{DL} . Co-ions on the contrary are repelled away from the wall. The capacitance at the wall is generally described by a Stern capacitance C_{Stern} from the inner immobile or specifically adsorbed layer and the outer diffuse layer capacitance C_{DL} . A value of $18 \frac{\mu F}{cm^2}$ is assumed for the Stern layer capacitance (i.e. considering an approximate thickness of 5 \AA and a dielectric constant of 10). The charge distribution is traditionally described by the Poisson-Boltzmann (PB) equation[32]:

$$\varepsilon \frac{\partial^2 \psi}{\partial x^2} = -2ze n_o \sinh \frac{(ze\psi)}{kT} \quad (9)$$

For a $z:z$ electrolyte, where the mobile diffusive charge is confined to a thin capacitor with a width governed by the Debye length.

$$\lambda_D = \sqrt{\frac{\varepsilon kT}{2z^2 e^2 n_o}} \quad (10)$$

Here z is the valency, n_o the bulk ion concentration, e the elementary charge, kT is the thermal energy and ε is the dielectric constant of the solvent. Equation (9) stems from a mean-field formulation where ions are treated as point charges, i.e., ion-ion and ion-wall interactions are ignored. In the conventional PB formalism, charge density generally blows up due to the

exponential dependence on surface potentials which is unrealistic under moderate to high ψ_o values. By accounting for close packing of ions at the interface, a limit is imposed on the maximum achievable charge density. In this work we model the NaCl system alone using the PB approximation since the effect of size was found to be negligible within the range of ψ_o obtained. However when dealing with multivalent ions the ion distribution from the interface is described using a 1:z approximation [34] including Steric effects (see Supplemental Material, Fig. S4). We find that Steric effects become prominent when considering large multivalent ions as layering and charge density saturation occurs for surface potentials $\sim 4-6\frac{kT}{e}$ (see Supplemental Material, Fig. S4).

Steric related phenomena are generally weak under low monovalent (NaCl) electrolyte concentrations and moderate σ_o conditions. Using the modeling framework presented in the previous section ion size effects were only marginally observed at E-fields above $\sim 0.5\frac{V}{nm}$ (not shown) with NaCl salts. We do however point out that in a recent theoretical study, Gillespie et al. [35] showed that with surface charge densities approaching $\sim 0.2\frac{C}{m^2}$ (which is typical of pristine dielectric interfaces) significant ion layering was observed even at low saline concentrations. It is thus paramount to understand the interfacial charge conditions as ion size effects can preclude a proper assessment of the observed signals with sensitive field effect devices. To accurately model ionic layering especially with multivalent salts, we invoke the modified Poisson-Boltzmann (MPB) theory [32, 36] [see Eq. (11)] which includes the hard-sphere Steric effect between ions owing to their finite size but ignores correlations. A Stern layer capacitance is not assumed in the MPB formulation.

$$\epsilon \nabla^2 \psi = -2ze n_\infty \frac{\sinh\left(\frac{ze\psi}{k_B t}\right)}{1 + 2\nu \sinh^2\left(\frac{ze\psi}{2k_B T}\right)} \quad (11)$$

where $\nu = 2a^3 n_0$ is the volume packing factor of ions and a is the size of the ion. The packing factor sets a limit on the maximum achievable charge density at the interface. The charge within the double layer is then given by

$$q_{MPB} = \sigma_{DL} = -\text{sgn}(\psi_{DL}) 2ze n_0 \lambda_D \sqrt{\frac{2}{\nu} \ln\left(1 + 2\nu \sinh^2\left(\frac{ze\psi_{DL}}{2k_B T}\right)\right)} \quad (12)$$

The electric field originating from the potential across the solid/electrolyte interface ($\psi_0 \geq \frac{kT}{e}$) attracts counterions to the surface forming an initial screening layer. If the surface potential rises further ($\sim 5 \frac{kT}{e}$), the electric field strength becomes high enough to cause layering of counterions against the solid interface (Supplemental Material, Fig. S4), leading to an effective increase in the double layer thickness, which extends further into the electrolyte bulk. From the capacitive point of view if one were to assume an additional Stern layer, C_{Stern} could help relieve the excess condensation of ions, but would not be able to withstand a large voltage drop $\sim 5-10 \frac{kT}{e}$ due to the Steric constraint. Under such field conditions, the region of ion accumulation extends away from the surface into the solution where ions do not exhibit specific interactions with the solid interface. This causes a further increase in the thickness of the double layer, leading to a decrease in the differential capacitance of the diffusive layer. As mentioned previously this effect becomes significant with large multivalent ions.

E. Multivalent ions and charge inversion

The Debye-Huckel (DH) approximation within the GCS double-layer framework states that the ionic screening effectively lowers the molecular charge in the electrolyte as observed from a finite distance. This is the net charge looking into the Gaussian sphere around the molecule [37] including its screening counter-ion cloud. In comparison with monovalent ions, multivalent ions are known to form a strongly correlated interface with charged moieties which overcharge the interface [38-43]. This can lead to excess counterion condensation and eventually polarity reversal, which cannot be explained by the conventional mean-field theory [32]. This counter-intuitive phenomenon is termed as charge inversion (CI) [38]. Shklovskii [38] postulated that this effect arose primarily due to strong lateral ion-ion interactions which got stronger as the valency increased, and a much larger negative electrochemical potential is developed within the 2D ionic layer. Ion-Ion correlations give rise to counterion layering against the interface, which can lead to overcharging under suitable field conditions. This is often much easier to achieve with multivalent ions [39] since the interaction energy between an ion and its background charge is directly proportional to $z^{3/2}$. Co-ions are then attracted to the interface to neutralize this excess counterion charge, which is the main reason for surface potential reversal. This effect can also lead to oscillations in the surface potential [38, 44]. Storey et al. [44] commented that in addition to Steric considerations, such correlation effects can affect the C_{DL} . In this work we do not model the effect of charge inversion but present experimental evidence in support of such a mechanism.

IV. RESULTS AND DISCUSSION

A. Nernstian vs. non-Nernstian surface

Before we describe the electrochemical gating response, we first highlight the difference between a Non-Nernstian and Nernstian surface. A Nernstian response implies that ψ_O vs. pH_B

response is linear and has a slope of $\sim 59mV / pH_B$. We find that the surface dissociation constants and net surface site density play dominant roles in determining this slope, and can shift the response from Nernstian to non-Nernstian. The pH_B response of an ISFET is traditionally given [38,39] by

$$\frac{\partial \psi_O}{\partial pH_B} = -2.3 \frac{kT}{e} \alpha \quad (13)$$

where α is defined as;

$$\alpha = \frac{1}{1 + \frac{2.3kTC_i}{e\beta_s}} \quad (14)$$

here $C_i = \frac{C_{DL} \cdot C_{Stern}}{C_{DL} + C_{Stern}}$, and from Eq. (3);

$$\beta_s = \frac{2.3 \cdot eN_s \cdot H_s^+ \cdot (K_b H_s^{+2} + K_a K_b 4H_s^+ + K_a K_b^2)}{(K_a K_b + K_b H_s^+ + H_s^{+2})^2} \quad (15)$$

The H_s^+ at the interface at PZC is given by

$$H_s^+ = \sqrt{K_a \cdot K_b} \quad (16)$$

It is immediately clear that a pH insensitive interface (non-Nernstian) necessarily implies a small β_s . Equation (14) suggests an intricate interplay between ΔpK and pH_B . A low value of ΔpK and high N_s is desired to achieve near Nernstian response [45, 46]. However the individual contributions of K_a and K_b are not immediately clear from Eq. (15). We note that both Bousse et al. [45] and Van den Vlekkert et al. [46] simplified Eq. (6) while deriving the pH sensitivity and showed that the surface potential close to the PZC can be described by the relation;

$$2.3(pH_{PZC} - pH_B) = \frac{e\psi_o}{kT} + \sinh^{-1}\left(\frac{e\psi_o}{\gamma kT}\right) \quad (17)$$

Here pH_{PZC} is defined by $\frac{(pK_a + pK_b)}{2}$, and $\gamma = \frac{2e^2 N_s}{C_{Diff} kT} \sqrt{\frac{K_a}{K_b}}$ is a dimensionless sensitivity parameter. In order to confirm this approximation and show that the pH sensitivity is strongly dependent on N_s and $\sqrt{\frac{K_a}{K_b}}$, without making simplifications, we first solve Eq. (13). We

observe that if K_b increases (pK_b is lowered), the surface has more neutral groups and hence pH_{PZC} extends into the acidic branch of the pH_B response. Lowering K_a (pK_a is increased) ensures the same effect, extending the PZC more towards the base branch. It is important to note that when pH_B is lower than pK_a , the surface will be mostly charge neutral and hence show a flat pH_B response. This is graphically represented in Fig. 2(a). However, when K_a increases, ΔpK decreases and the response becomes more Nernstian. This is in agreement with the simplification by Bousse et al. [45] [see Eq. (17)] and earlier reports on chemical surface modifications [47].

A smaller ΔpK creates more charged groups around the PZC, which improves the pH_B response. Lowering N_s reduces α and the slope of the pH_B response, because a reduction in the number of ionizable groups decreases the net available sites for proton binding [Fig. 2(b)]. The PZC however does not change with varying N_s .

B. Electrochemical gating

As previously mentioned, E_{OX} will induce σ_o and σ_{DL} which together set ψ_o . For an interface exhibiting a single ionizable group (the single- pK model), σ_o first responds to E_{OX} until all

charges (N_s) have responded [9]. During this process ψ_o does not change and the surface is said to be “buffering”. However, in many cases with amphoteric interfaces such as Al_2O_3 and SiO_2 , the nature of the buffering strongly depends on ΔpK and N_s . The choice of $pK_a = 10$ and $pK_b = 5$ for the present polysilicon interface under consideration represents a non-Nernstian surface with a pH_{PZC} around $pH_B = 7.5$. This corresponds to low pH sensitivity in the given ΔpK range and hence extremely low buffering. In Fig. 2(c&d), we compare the change in ψ_o for varying E_{OX} at different pH_B and n_o values. A slight skewing is observed [Fig. 2(c)]. Buffering is rather weak for intermediate pH values close to the PZC but gets stronger at extreme pH values. The skewing (slight sigmoid tendency) indicative of buffering is tunable as a function of E_{OX} . In Fig. 2(d), we notice that the maximal change in ψ_o with E_{OX} is strongest for the lowest n_o , in agreement with the results of Jiang and Stein[9]. This is because at low n_o , very little charge is available to screen a given modulation in ψ_o or σ_o , while at high n_o a small shift in σ_o can cause large changes in σ_{DL} and hence a substantial swing in ψ_o is energetically unfavorable.

Under negative E_{OX} conditions we notice that varying pK_b [Fig. 2(e)] modulates the surface potential even at zero E_{OX} . Such changes in surface ionizability can be achieved by suitable self assembled monolayer (SAM) formations [47]. If we flip the surface constants, i.e. $pK_a = 10$ and $pK_b = 5$, maximal buffering is observed within the ΔpK range indicating a Nernstian pH response [Fig. 2(f)]. As previously mentioned, the effect of the ion size was weak for NaCl salts in these simulations as ψ_o never rose above $\sim 4 - 5 \frac{kT}{e}$. The above simulations show that in

addition to pH and bulk salinity E_{OX} can be tuned to affect the properties of the interface to a desired region of operation.

C. EOS capacitance-voltage (CV) measurements

Polysilicon-Oxide-Silicon capacitors were fabricated as described earlier. V_{REF} was swept from $-10V$ to $+10V$. At $-10V$, the silicon was in accumulation (positive interface charge). As V_{REF} was swept positive, the charge in silicon was depleted, and finally at $+10V$ it was inverted. The effect of the double layer modulation or pH_B on the surface potential is that the DC operating point is affected, which shifts the flat-band voltage (V_{FB}) of the capacitor stack [Fig. 3(a)]. In Fig. 3 we chose to plot only the transition region and not the entire range of the V_{REF} sweep.

A linear response in V_{FB} with respect to pH_B variation was noticed ($\sim 50mV/pH$) when sweeping V_{REF} from $-10V$ to $+10V$. A strong hysteresis effect was observed when V_{REF} was cycled from $-10V$ to $+10V$ and back to $-10V$ as shown in Fig. 3(a), for $pH_B = 7$ and $pH_B = 9$. This hysteretic effect got slightly larger with decreasing pH_B (not shown) and was found to be strongly dependent on the type of interface. For example, we found that both Al_2O_3 and poly-Si interfaces showed distinct hysteresis [48, 49] while thermal SiO_2 showed a negligible hysteresis upon exposure to pH solutions (not shown). Since E_{OX} can influence σ_o similar to the effect of pH_B , as described earlier (Fig. 2), the varying DC sweep affects the ionization state of the interface which in turn affects surface recovery. When V_{REF} is swept from $-10V$ to $+10V$, the field in the oxide in the beginning promotes anion adsorption or interface deprotonation and results in a negative σ_o . This deprotonation effect is strongly dependent on the choice of pK_a and pK_b . As the forward sweep proceeds towards $+10V$, this negative charge is poorly

neutralized due to a small β_S , which renders a higher V_{FB} . On the reverse sweep, the surface is completely protonated or neutralized and hence σ_o is more positive. This $+\sigma_o$ only dissociates over the time course of the sweep, resulting in a lower V_{FB} . The hysteresis is similar to the trap charge effect in electronic devices. In order to confirm that this hysteretic effect is indeed mostly due to protons instead of ions, we performed CV sweeps at different n_o at $pH_B = 7$ and found that the hysteretic window was almost independent of n_o . V_{FB} increased by $\sim 30\text{mV}$ when n_o varied from $100\mu\text{M}$ to 1mM but then slightly decreased upon further n_o increase [Fig. 3(b)]. This slight dependence of ψ_o on n_o is attributed to β_S . The sensitivity of σ_o to changes in the bulk electrolyte can be estimated by [4]

$$\sigma_o = C_i \cdot \psi_o = -\sigma_{DL} \quad (16)$$

where C_i is the total capacitance seen by the interface:

$$C_i = \frac{C_{DL} \cdot C_{Stern}}{C_{DL} + C_{Stern}} \quad (17)$$

Here σ_{DL} is the charge in the double layer, and C_{Stern} is the Stern layer capacitance which is generally considered immobile. A change in n_o directly affects σ_o via σ_{DL} [Eq. (16)] which in turn affects C_{DL} and ψ_o self-consistently. The Boltzmann relation in Eq. (7) directly implies that a change in ψ_o affects H_S^+ . However, the surface buffering capacity β_S will try to maintain H_S^+ constant by ensuring a new surface chemical equilibrium satisfied by Eq. (8). If β_S is small, C_{DL} can strongly regulate ψ_o [4], where the surface is maximally sensitive to ions and least sensitive to pH.

In order to further validate field-dependent ionic activity, we also varied the $\frac{z}{V}$ (valency/volume) ratio of the cation. Ionic size and valency play a crucial role in the double layer formation [32, 50]. Hence field-induced double layer modification serves as a suitable control to validate electrochemical response over the electrolyte interface. Size and valency sets a constraint on the width of the double layer which is strongly surface potential dependent (see Supplemental Material). When V_{REF} was swept from $-10V$ to $+10V$ we observed a reduction in V_{FB} when $MgCl_2$ replaced $NaCl$ in the electrolyte but a slight increase in V_{FB} when $Co(NH_3)_6Cl_3$ replaced $MgCl_2$ [Fig. 3(c)]. For the latter, this effect was accompanied by a corresponding decrease in the accumulation capacitance C_{acc} , while with $MgCl_2$, C_{acc} increased. We attribute the decrease in capacitance with $Co(NH_3)_6Cl_3$ to the Steric effect, which imposes packing constraints on the thickness of the condensed ionic layer and the effective C_{Stern} . It however appears that under the given field conditions and concentrations of $MgCl_2$ used the Steric effect factor is less dominant.

However, the net reversal in ψ_o observed with the trivalent cations cannot be accounted for solely by the Steric effect. ψ_o reversal is possible with trivalent ions even at extremely low n_o [39] primarily due to electrostatic correlations. This seems to suggest that the predominant factors that determine the onset of potential reversal are the ionic $\frac{z}{V}$ ratio and strong ion-ion interaction between multivalent ions. Revealing the interdependence between n_o and the $\frac{z}{V}$ ratio is currently work in progress and will be reported in the future.

D. CvMOS – transient responses

Figure 4(a-f) summarizes the transient responses of the CvMOS for varying n_o under different pH_B conditions of 11, 7 and 3. The electrolyte bulk was held constant at 0.8V with respect to the source at ground. The CG pulse train was switched between +15V and -15V while reading intermittently at +10V. The drain bias V_D was held at 1V throughout the experiment. When a +15V CG bias was applied, I_D increased. However, the field in the SG oxide (E_{SG_ox}) during the rising pulse became more positive looking into the electrolyte. This immediately resulted in a net negative charge in solution by a combination of σ_o and σ_{DL} . When the CG was re-biased to +10V, the $-\sigma_o$ induced during the previous +15V application remained at the surface (hysteresis). This caused the I_D between 110 – 170 seconds to be smaller than the initial 0 – 55 seconds. On application of a -15V CG bias, E_{SG_ox} became negative and caused a net positive charge building up at the SG interface which enhanced H^+ adsorption. When the CG was re-biased to +10V between 230 – 285 seconds, I_d was higher than the initial readout state between 0 – 55 seconds [dotted line in Fig. 4(b)]. In order to confirm that protonation was the dominant effect during and after the negative gating period, we performed experiments in the presence and absence of a competing solution buffer (TRIS) [Supplemental Material, Fig. S5(b)] at $pH_B=7$. In the presence of TRIS, no increase in current was observed after application of the -15V CG pulse. In the absence of electrolyte and with the SG directly probed to ground [Supplemental Material, Fig. S5(c)], the transient current recording showed no variation after +10V, +15V and -15V CG bias application. This strengthens the assertion that no charge was either injected or erased into the FG during the CG bias application and the main reason for the observed differences in current levels is surface charge regulation.

For $pH_B=11$, the surface was already buffering [Fig. 4(d)] within the experimental E_{SG_OX} range (*the un-shaded region*). We observed that ψ_o was negative in the beginning, close to the zero E_{SG_OX} condition. With increasing n_o , ψ_o became more positive, which was reproduced in the transient response [Fig. 4(a)] reflected by a higher I_D for increasing n_o within the initial 0 – 60 seconds. After application of a $-15V$ CG pulse between 170 - 230 seconds, however, we observed a recovery to higher I_D and a longer settling time with decreasing n_o . We attribute this to an increased hysteretic effect possibly due to increased cation adsorption at high pH_B . This coupled with a larger surface potential shift at lower n_o can potentially lead to different rates of surface re-equilibration. Quantification of cation adsorption under such conditions however is difficult to decouple and is at present a measurement challenge. At $pH_B = 7$, however the surface potential was closer to zero around the readout condition of $E_{OX} \sim 0.01V/nm$. The model dictated a reversal in ψ_o [Fig. 4(e)] when E_{SG_OX} toggled between positive and negative values. This was experimentally observed in Fig. 4(b) with opposite shifts in I_D after the $+15V$ and $-15V$ CG pulses in comparison with the initial 0 – 60 seconds. This clearly showed that although during readout E_{SG_OX} was close to zero, the carryover net charge and ψ_o from the previous CG pulse remained and thus the gated surface state was observed. At $pH_B = 3$, ψ_o was highly positive [Fig. 4(f)] to begin with and increased with decreasing n_o . I_D was also found to increase after gating by positive and negative fields [Fig. 4(c)].

E. CvMOS – quasi-static response

Figure 5(a) summarizes the pH response of the CvMOS in terms of the V_{th} shifts observed from CG (V_{th_CG}). ψ_o was calculated via Eq. (1) after extracting the capacitive amplification ratio

experimentally [Supplemental Material, Fig. S6(a)]. The pH_B response showed a non-Nernstian characteristic with a clear plateau around $pH_B = 8$ (i.e. pH_{PZC}). Increasing n_o lowered ψ_o at low pH_B but enhanced ψ_o slightly at high pH_B . This is consistent with the notion that ion adsorption plays little role in shifting ψ_o at physiologically relevant pH_B , because the opposite would have meant an increase in ψ_o due to Cl^- ion binding. Also as n_o increases, the surface buffering property decreases and hence affects the overall pH_B response. This can be understood from Eq. (13) and specifically by closely examining the sensitivity parameter α . It is immediately clear that a small β_s competes with C_i and determines the overall pH_B response as a function of n_o . At high n_o , C_i is much larger than β_s and hence results in a reduced pH_B response. At high pH_B the slight increase in ψ_o with varying n_o can be attributed to simultaneous H^+ and Na^+ ion binding [48]. This range of pH_B however is too small to establish a meaningful conclusion. It is quite clear that changing n_o does have an influence on β_s and ψ_o primarily from the buffering perspective. We do however point out that n_o would affect ψ_o even for surfaces that are uncharged or exhibit a constant charge condition. This would then primarily occur due to the change in C_i . Figure 5(b) provides a fit to the experimental pH_B response using the $2pK$ model presented earlier. A pK_b of 5.0 and pK_a of 10.0 was extracted. Figure 5(c&d) shows the simulated effect of E_{OX} induced gating on the pH_B response for two distinct combinations of pK_a and pK_b . In both cases the pH_{PZC} shifts to higher pH values as E_{OX} increases. However for the non-Nernstian interface where pK_b is lower than pK_a [Fig. 5(d)], the shift in pH_{PZC} is much higher (*horizontal arrow*). The pH insensitive region for this

surface moves towards lower pH_B values as E_{OX} increases (*dotted arrow*). This shows that the effect of E_{OX} is similar to varying pH_B as both can tune σ_O . E_{OX} serves as an electrical factor, while pH_B as a chemical factor. We also experimentally observed this electrochemical gating effect by injecting charges onto the FG. We applied a CG bias of $\sim 40V$ for approximately 30 seconds while holding V_{REF} at 0V. Due to the larger capacitive coupling from SG, V_{FG} remained closer to V_{REF} and did not rise by more than 4~5V. E_{CG_OX} during this pulse period promoted FN tunneling which resulted in a net positive Q_{FG} . It is important to note that in the present study, with the given geometry constraints, E_{SG_OX} potentially achieved values of 0.02–0.2V/nm when $Q_{FG} \sim 8 - 20 pC$. A quick (15 seconds) CG ramp was used to monitor the new surface charge state. We found that with $+Q_{FG}$ present, the pH_B response was dramatically affected and the pH insensitive region moved to lower pH_B , which resulted in an overall reduced pH response [Fig. 5(e)], which is in line with the simulation result shown in Fig. 5(d). The surface model also dictates that by reducing the density of surface hydroxyl groups, the pH_{PZC} shift was more pronounced [Fig. 5(f)]. Taken together the CV, IV and transient responses suggest that surfaces exhibiting a non-Nernstian response with large ΔpK will undergo a hysteresis in a saline environment. Ion adsorption does play a role under certain pH_B conditions [48, 49] but a better treatment of the site binding parameters is needed to account for such subtle effects.

F. CvMOS – programming response and the role of the reference electrode

We recall that V_{FG} is influenced by ψ_O which is pH_B and C_{DL} dependent. Also from the transient measurements it is clear that at small positive CG pulses the net carry-over charge is negative. Hence as V_{CG} is initially increased, V_{FG} perturbs ψ_O inducing a net $-\sigma_O$ which couples

back to influence the transistor current. As V_{CG} is further increased V_{FG} does not rise as high due to the influence of V_{REF} . The E_{CG_OX} increases favoring FN tunneling [28] to create a net positive Q_{FG} , reducing V_{th} measured from the CG [Fig. 6(a)]. V_{FG} is more positive as the tunneling process ensues due to the positive Q_{FG} [Supplemental Material, Fig. S6(c)]. This would necessarily imply that E_{CG_OX} lowers and E_{SG_OX} increases. The total threshold voltage shift (V_{th_CG}) is attributed to Q_{FG} and its net effect on $\sigma_{DL} + \sigma_O$. We reiterate that during tunneling, there is no charge leakage into the solution as measured in control experiments (not shown). When the reference electrode is floated, however, the capacitive coupling dramatically reduces and the FG is no longer pulled to a defined electrolyte potential. This ensures that V_{FG} rises with V_{CG} with increasing E_{TOX} to promote electron injection ($-Q_{FG}$) into the FG, thereby increasing the V_{th} measured from the CG [Supplemental Material, Fig. S6(b)]. This operation is particularly significant when attempting to manipulate charged biomolecules such as DNA as reported in part II.

In order to confirm the interplay between σ_{DL} and Q_{FG} , we performed experiments by changing n_O and hence C_{DL} . We found that C_{DL} strongly influenced the tunneling characteristics [Fig. 6(a)]. As C_{DL} lowered so did the V_{REF} coupling to the FG. This caused V_{FG} to rise higher with V_{CG} which lowered electron out-tunneling and favored electron in-tunneling, and hence resulted in a smaller net Q_{FG} after $V_{CG} > 30V$. The small initial increase in ΔV_{th} at low to moderate CG voltages is attributed to surface deprotonation and a net remnant negative ψ_O when V_{CG} is too low to cause tunneling.

In many experiments involving cell suspensions and biomolecules, the electrolyte composition is never just composed of single monovalent salts. In order to further develop the gating concept and corroborate the CV measurements, we performed experiments keeping n_o constant at 20mM and varying the cationic $\frac{z}{v}$ ratio [Fig. 6(b)]. We observed that in the vicinity of the knee point [denoted by the arrow in Fig. 6(b)] where tunneling had just begun, the reduction in V_{th} was slightly more pronounced for $Co(NH_3)_6Cl_3$ in comparison to $NaCl$ and $MgCl_2$. This result shows that with $Co(NH_3)_6Cl_3$ present, ψ_o increased just after the programming pulse application. That is, it became more positive with $+Q_{FG}$. This finding is in line with the +10V to -10V V_{REF} (reverse) sweep performed during CV analysis [Fig. 3(c)] in which ψ_o was observed to be more positive (lower V_{FB}) with $Co(NH_3)_6Cl_3$. It is important to note that E-fields with similar strength and polarity are developed in the underlying oxide either under $+Q_{FG}$ conditions in the CvMOS or low to moderate $-V_{REF}$ application in the EOS structure. Taken together experimental evidence suggests field induced surface potential reversal due to a combination of both C_{DL} lowering and correlation effects [51] when experimenting with trivalent salts. This effect was not observed with monovalent or divalent salts. In Fig. 6(b), the overall magnitude of ΔV_{th} was also found to be lower for $Co(NH_3)_6Cl_3$. This is again consistent with the notion that C_{DL} affects the net Q_{FG} [Fig. 6(a)], and is in accordance with the CV measurements presented earlier in which C_{DL} was found to reduce for trivalent salts.

V. CONCLUDING REMARKS

We presented the dynamic surface charge modulation of a solid-electrolyte interface, and the concept of surface pH tuning. By modulating the polarity of stored charge, one can switch

between a pH sensitive condition and a non-Nernstian surface. Transistor and EOS capacitor measurements are compared and a 2-pK model with surface charge regulation is presented. We conclude that proton adsorption and desorption is the primary reason for hysteresis at such interfaces, which also provides a method of probing the surface charge state. Quasi-static I-V measurements, CV profiles and high resolution transient recordings are presented to corroborate our findings.

Acknowledgements

This work was supported by NSF MRSEC Grant DMR 0520404 through Cornell Center for Materials Research (CCMR) Interdisciplinary Research Group (IRG). We would like to thank Prof. Lois Pollack for providing valuable insights during the course of this study. We acknowledge the Nano Biotechnology Center (NBTC) at Cornell and the Cornell Nano-Scale Facility (CNF) for allowing us to use their facilities. K.J would like to thank Lihua Wang and Suzette A. Pabit for help with electrolyte preparation.

Supplemental Material: Supplementary material accompanies this article.

References

- [1] F. Uslu *et al.*, Biosens. Bioelectron. **19**, 1723 (2004).
- [2] S. Ingebrandt *et al.*, Biosens. Bioelectron. **22**, 2834 (2007).
- [3] N. Zehfroosh, M. Shahmohammadi, and S. Mohajerzadeh, Electron Device Letters, IEEE **31**, 1056 (2010).
- [4] R. E. G. van Hal, J. C. T. Eijkel, and P. Bergveld, Sens. Actuators, B **24**, 201 (1995).
- [5] S. Chen *et al.*, Nano Lett. **11**, 2334 (2011).
- [6] O. Knopfmacher *et al.*, Nano Lett. **10**, 2268 (2010).
- [7] P. Bergveld, Sens. Actuators, B **88**, 1 (2003).
- [8] I. Y. Wong, M. J. Footer, and N. A. Melosh, Soft Matter **3**, 267 (2007).

- [9] Z. Jiang, and D. Stein, *Langmuir* **26**, 8161 (2010).
- [10] R. B. H. Veenhuis *et al.*, *Lab on a Chip* **9**, 3472 (2009).
- [11] K. Ghowsi, and R. J. Gale, *J. Chromatogr. A* **559**, 95 (1991).
- [12] R. B. M. Schasfoort *et al.*, *Science* **286**, 942 (1999).
- [13] R. Karnik, K. Castelino, and A. Majumdar, *Appl. Phys. Lett.* **88**, 123114 (2006).
- [14] R. Fan *et al.*, *Phys.Rev.Lett.* **95**, 086607 (2005).
- [15] W. Guan, R. Fan, and M. A. Reed, *Nat Commun* **2** (2011).
- [16] K. Horiuchi, and P. Dutta, *Lab on a Chip* **6**, 714 (2006).
- [17] H. Daiguji, T. Adachi, and N. Tatsumi, *Phys.Rev.E* **78**, 026301 (2008).
- [18] E. B. Kalman, I. Vlassiuk, and Z. S. Siwy, *Adv. Mater.* **20**, 293 (2008).
- [19] Y. Liu *et al.*, *Appl. Phys. Lett.* **97**, 143109 (2010).
- [20] Y. He *et al.*, *ACS Nano* **5**, 5509 (2011).
- [21] Z. Jiang, and D. Stein, *Phys.Rev.E* **83**, 031203 (2011).
- [22] W. R. McKinnon, D. Landheer, and G. Aers, *J. Appl. Phys.* **104**, 124701 (2008).
- [23] N. Y. M. Shen *et al.*, *IEEE Trans. Electron Devices* **50**, 2171 (2003).
- [24] T. Shibata, and T. Ohmi, *IEEE Trans. Electron Devices* **39**, 1444 (1992).
- [25] J. Go *et al.*, *ACS Nano* **6**, 5972 (2012).
- [26] J. Go, P. R. Nair, and M. A. Alam, *J. Appl. Phys.* **112**, 034516 (2012).
- [27] Rino Micheloni, Luca Crippa, and A. Marelli, *Inside NAND Flash Memories* (Springer New York, 2010).
- [28] F. Masuoka *et al.*, *Solid-State Circuits, IEEE Journal of* **22**, 548 (1987).
- [29] C.-Y. Hsiao *et al.*, *Biosens. Bioelectron.* **24**, 1223 (2009).
- [30] G. Wenga *et al.*, *Biosens. Bioelectron.* **40**, 141 (2013).
- [31] R. Tsu, and L. Esaki, *Appl. Phys. Lett.* **22**, 562 (1973).
- [32] M. S. Kilic, M. Z. Bazant, and A. Ajdari, *Phys.Rev.E* **75**, 021502 (2007).
- [33] J. C. van Kerkhof, J. C. T. Eijkel, and P. Bergveld, *Sens. Actuators, B* **18**, 56 (1994).
- [34] D. Ben-Yaakov *et al.*, *J. Phys.: Condens. Matter* **21**, 424106 (2009).

- [35] D. Gillespie *et al.*, J. Colloid Interface Sci. **359**, 520 (2011).
- [36] I. Borukhov, D. Andelman, and H. Orland, Phys.Rev.Lett. **79**, 435 (1997).
- [37] J. A. Grant, and B. T. Pickup, J. Phys. Chem. **99**, 3503 (1995).
- [38] B. I. Shklovskii, Phys.Rev.E **60**, 5802 (1999).
- [39] F. H. J. van der Heyden *et al.*, Phys.Rev.Lett. **96**, 224502 (2006).
- [40] R. Qiao, and N. R. Aluru, Phys.Rev.Lett. **92**, 198301 (2004).
- [41] A. Y. Grosberg, T. T. Nguyen, and B. I. Shklovskii, Rev.Mod.Phys. **74**, 329 (2002).
- [42] K. Besteman, M. A. G. Zevenbergen, and S. G. Lemay, Phys.Rev.E **72**, 061501 (2005).
- [43] K. Besteman *et al.*, Phys.Rev.Lett. **93**, 170802 (2004).
- [44] B. D. Storey, and M. Z. Bazant, Phys.Rev.E **86**, 056303 (2012).
- [45] L. Bousse, N. F. de Rooij, and P. Bergveld, IEEE Trans. Electron Devices **30**, 1263 (1983).
- [46] H. van den Vlekkert, L. Bousse, and N. de Rooij, J. Colloid Interface Sci. **122**, 336 (1988).
- [47] A. van den Berg *et al.*, Sensors and Actuators **8**, 129 (1985).
- [48] L. Bousse, N. F. De Rooij, and P. Bergveld, Surf. Sci. **135**, 479 (1983).
- [49] A. Tarasov *et al.*, ACS Nano **6**, 9291 (2012).
- [50] D. Ben-Yaakov *et al.*, Curr. Opin. Colloid Interface Sci. **16**, 542 (2011).
- [51] T. T. Nguyen, and B. I. Shklovskii, Phys.Rev.E **64**, 041407 (2001).
- [52] See Supplemental Material at [] for additional details of the physical principles that describe the device operation, control experiments that support details presented in the main text, simulation of the tunneling operation and Table outlining the equation set describing the working of the *CvMOS* transistor.

Figure Captions

FIG. 1. (a) (Color online) The EOS capacitor used in the CV analysis. (b) The CvMOS transistor with two independently driven gates: (control) CG and (sensing) SG coupled to a common (floating gate) FG. The FG to electrolyte capacitive coupling is mimicked by the EOS structure. The CG is shielded from the solution via a thick oxide (2 μ m) passivation. (c) An SEM image of the fabricated transistors showing the SG, CG and transistor regions, respectively.

FIG. 2. (a) (Color online) Variation in ψ_o as a function of pH_B for variations in ΔpK . As ΔpK increases (arrow) the slope becomes more non-Nernstian (lower than 60mV/pH). (b) ψ_o vs. pH_B for variations in surface site density in m^{-2} . The relative flattening in the response increases as N_s decreases. Arrow indicates direction of N_s decrease. (c) ψ_o vs. E_{OX} for varying pH_B . Solid arrow represents direction of decreasing pH_B . When pH_B is in the range between the $2pK$'s, the surface buffering is low with $pH_{PZC} \sim 7$. Here $pK_a = 10$ and $pK_b = 5$. The region between the dotted lines represents the E_{OX} range used in this study and the dark shaded region represents the fields applicable during readout. (d) ψ_o vs. E_{OX} for varying salinity n_o . The shaded region (grey) represents field during readout. Solid arrow represents the direction of increasing n_o . The maximum modulation in ψ_o occurs for lower n_o . At the zero E_{OX} condition, the surface sensitivity to varying n_o is negligible. An applied positive or negative E_{OX} can tune ψ_o to be sensitive to changes in n_o . (e) ψ_o vs. E_{OX} for varying pK_b . ψ_o is affected only in the $-E_{OX}$ region. Solid arrow represents the direction of increasing pK_b . (f) ψ_o vs. E_{OX} for varying pH_B with pK_a and pK_b flipped. Solid arrow represents the direction of increasing pH_B . Maximal buffering (dotted arrow) is observed in the range between the $2pK$'s.

FIG. 3. (Color online) Experimental CV analyses depicting V_{FB} shifts for, (a) varying pH_B . A strong pH_B -dependent hysteresis is observed while performing cyclic sweeps. A lowering in V_{FB} is observed when the reference electrode is swept from positive to negative voltages (indicated by arrow/circle) implying a net positive remnant surface charge (b) varying bulk ion concentration (n_o). The hysteretic window at constant pH_B is insensitive to n_o while the accumulation region capacitance is dependent on n_o and (c) varying cationic valency (z). Varying (z) influences the double layer composition which further influences σ_o . Divalent cations shift the V_{FB} lower while trivalent ions induce a slight increase. C_{DL} is lower for the trivalent cations. Here (R) denotes the reverse sweep in (a-c).

FIG. 4. (Color online) Transient recordings under CG pulse trains. Drain current output as a function of varying n_o at (a) $pH_B = 11$, (b) $pH_B = 7$ and (c) $pH_B = 3$. The pulse train amplitude and duration are shown under each figure. Calculated ψ_o as a function of E_{OX} for varying n_o for (d) $pH_B = 11$, (e) $pH_B = 7$ and (f) $pH_B = 3$, using $pK_a = 10$ and $pK_b = 5$. At $pH_B = 11$, ψ_o is net negative for E_{SG_OX} close to $0 \frac{MV}{cm}$ and becomes more negative with decreasing n_o . This is reflected in the current levels during the transient recordings. At $pH_B = 7$ the current levels flip when E_{SG_OX} is switched from positive to negative since ψ_o is positive at the positive E_{OX} and negative at negative E_{OX} . At $pH_B = 3$, ψ_o is net positive and increases with decreasing n_o . In all three cases, the drain current is higher between 230 – 285 seconds than the initial state between 0

and 60 seconds. This is attributed to net positive charge due to field-induced protonation which remains after the negative gating pulse is relaxed. This is similar to the observed hysteresis in Fig. 3. The regions between the dotted lines in (d-f) represent the fields during readout. Solid arrows in (d-f) represent the direction of increasing n_o .

FIG. 5. (Color online) (a) ΔV_{th} (Representative of ψ_o) as a function of pH_B for varying n_o . The slope of the pH_B response reduces in the range between pK 's while it increases at extreme pH_B values. Cations are presumed to contribute to the slight increase in ψ_o at high pH_B . Arrow indicates increasing order of n_o (b) Theoretical fit to the experimental pH_B response reveals ΔpK of 5 for a given surface site density of $10^{17} m^{-2}$. ψ_o vs. pH_B for varying E_{OX} with (c) $pK_a < pK_b$ and (d) $pK_a > pK_b$. Both responses indicate a shift in pH_{PZC} (star) towards higher pH_B as E_{OX} is increased while the pH insensitive region shifts towards higher pH_B (c) and lower pH_B (d), with increasing E_{OX} respectively. This is primarily due to the different ionization states of the surface dependent on the choice of pK_a and pK_b . (e) Experimentally extracted pH_B response as a function of positive E_{OX} in the SG oxide, achieved by $+Q_{FG}$. Results show the pH insensitive region shifts towards lower pH_B . Error bar represents average over 3 experimental runs. (f) ψ_o vs. pH_B for varying E_{OX} with $pK_a > pK_b$ and lower N_s ($5 \times 10^{16} m^{-2}$). The modulation in pH_{PZC} is a lot more exaggerated.

FIG. 6. (Color online) ΔV_{th_CG} as a function of the CG pulse amplitude for variations in (a) n_o for a NaCl electrolyte and (b) cationic valency for CvMOS with an amplification ratio of 20 at a bulk n_o of 20mM. An initial increase in ΔV_{th} at low to moderate CG voltages is attributed to surface deprotonation and a net remnant negative ψ_o . Due to asymmetric CG and SG capacitances, V_{FG} is pulled closer to V_{REF} . This ensures that at sufficiently high V_{CG} the V_{FG} does not rise much which leads to large E_{CG_OX} for FN tunneling. Reduction in n_o and C_{DL} weakens the coupling between the FG and V_{REF} , causing E_{CG_OX} and net Q_{FG} to reduce. Varying cationic valency indicates more pronounced shifts in ΔV_{th_CG} around the knee point (i.e. where tunneling begins) (shown by dotted arrow) especially with trivalent salts in comparison to mono and divalent salts. A decrease in the overall ΔV_{th_CG} with trivalent salts upon tunneling is consistent with the notion that C_{DL} is also decreasing. Error bars represent an average over 3 experimental runs.

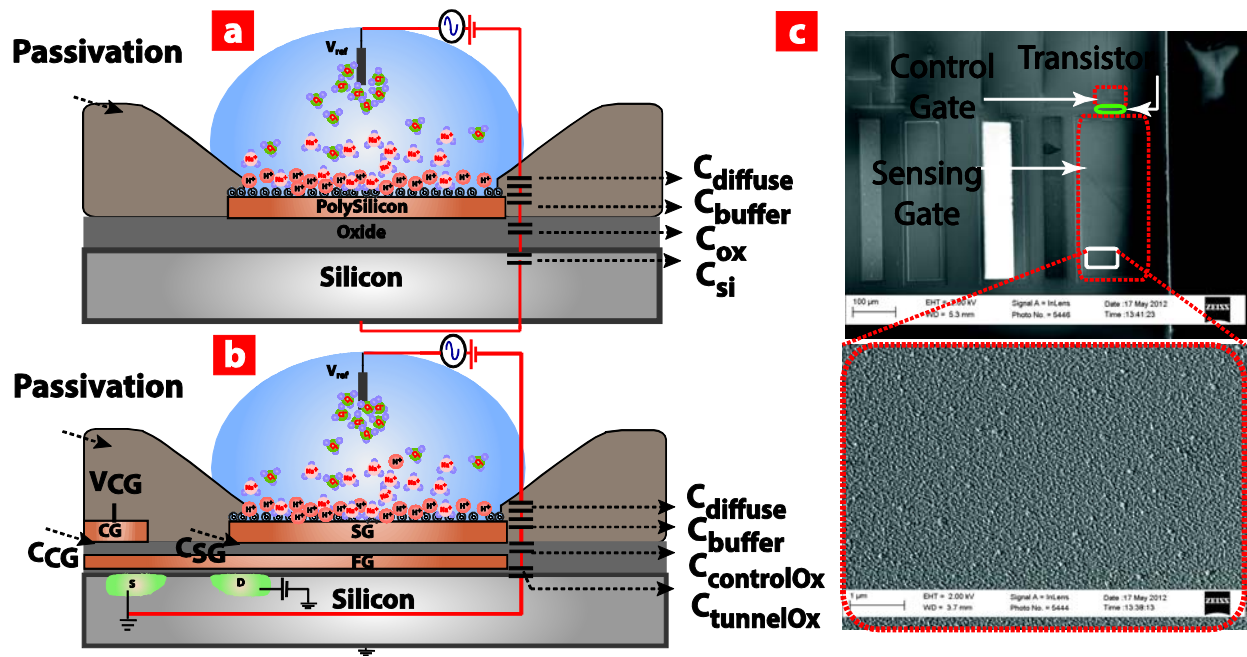


FIG. 1

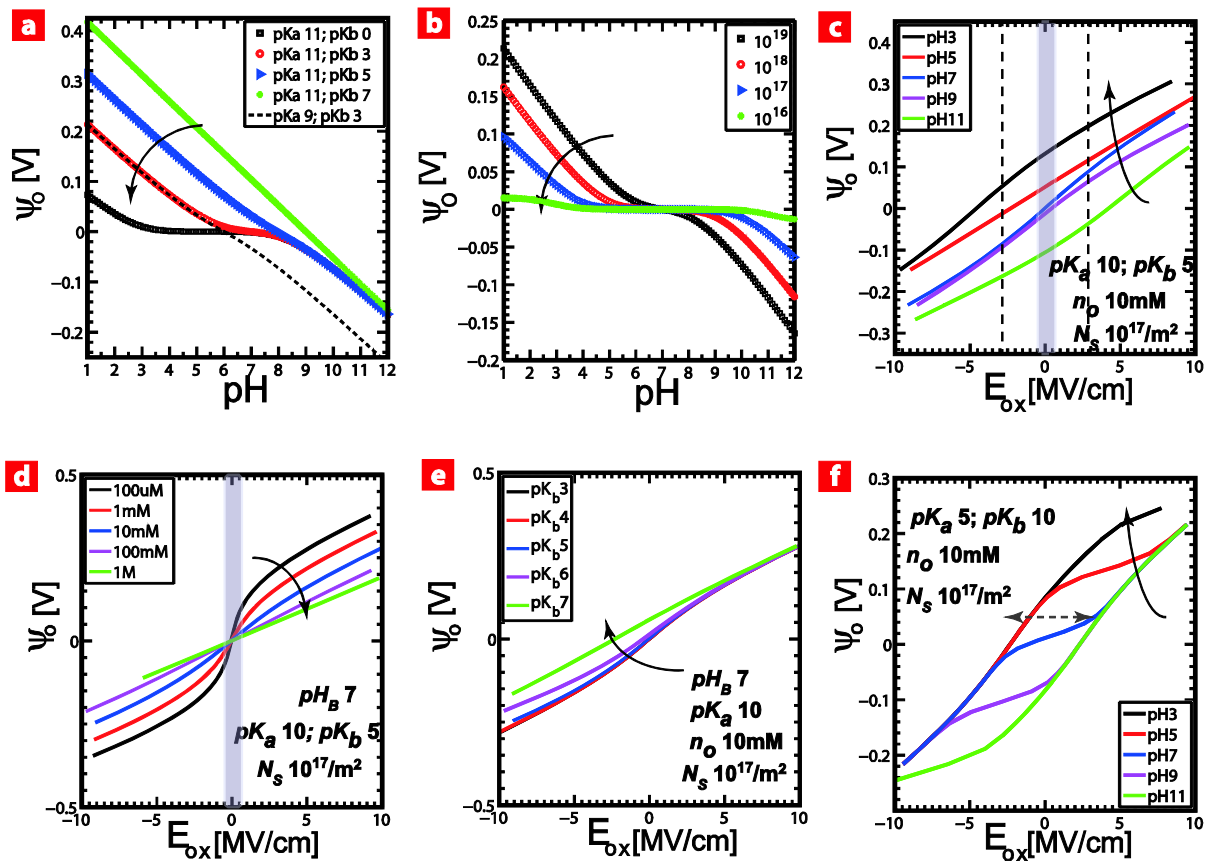


FIG. 2

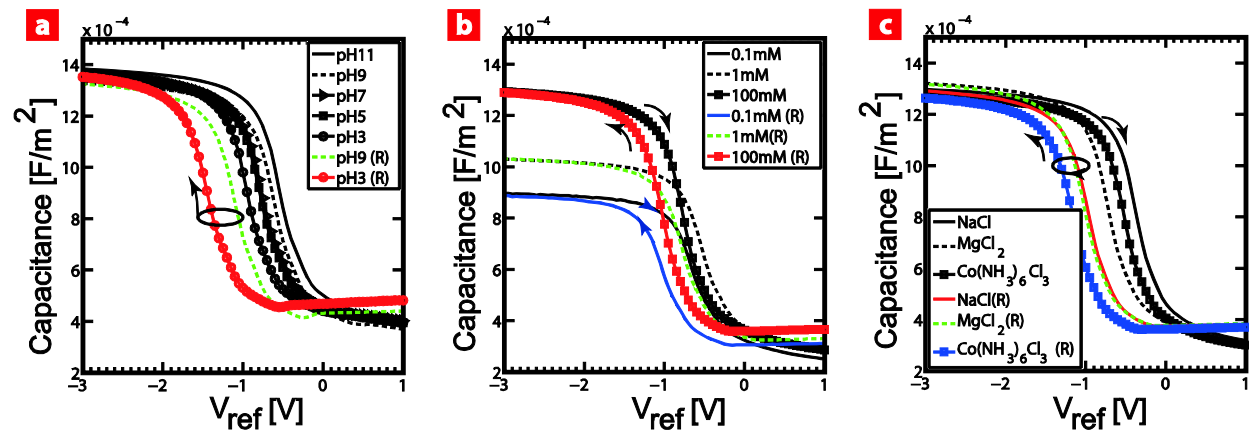


FIG. 3

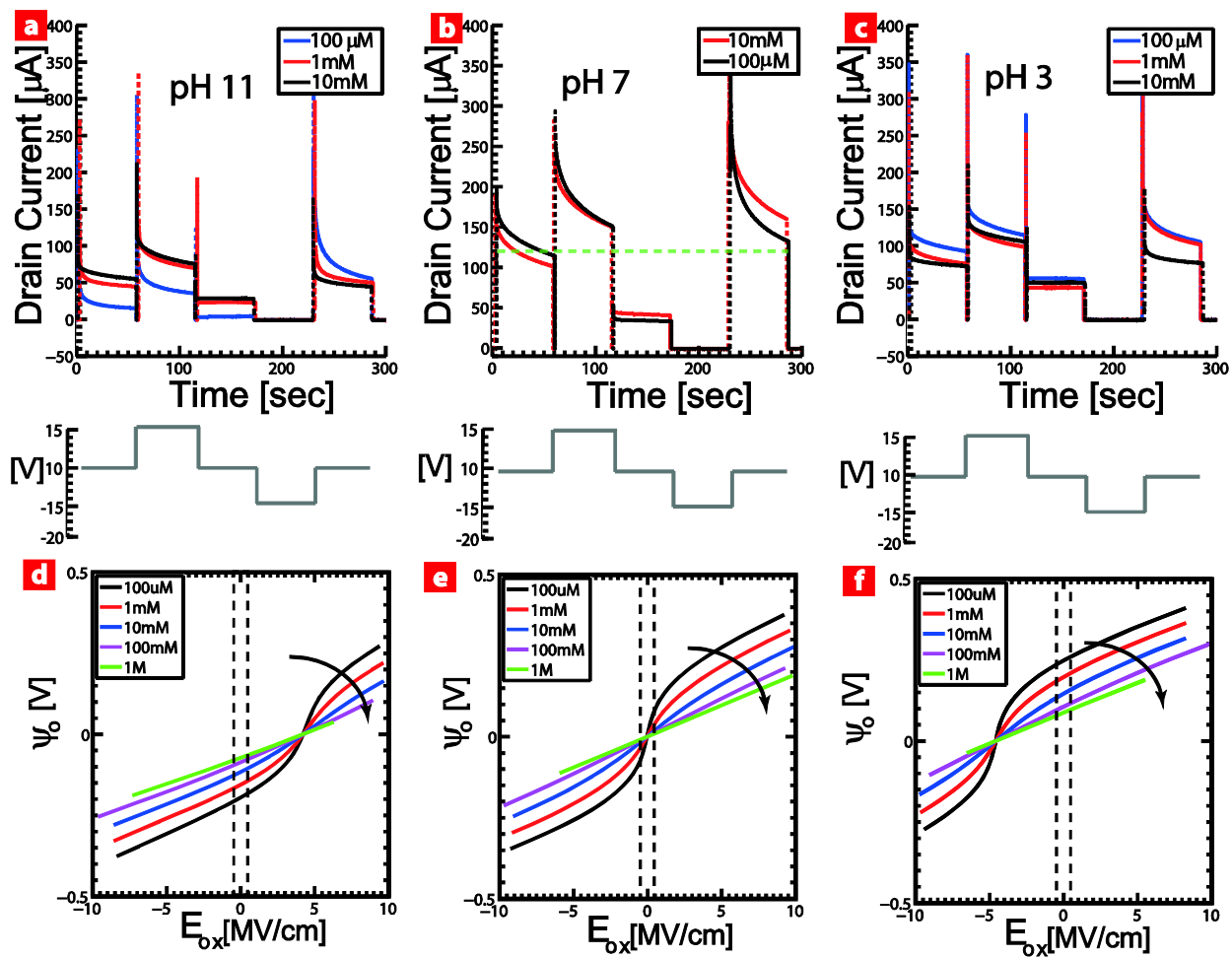


FIG. 4

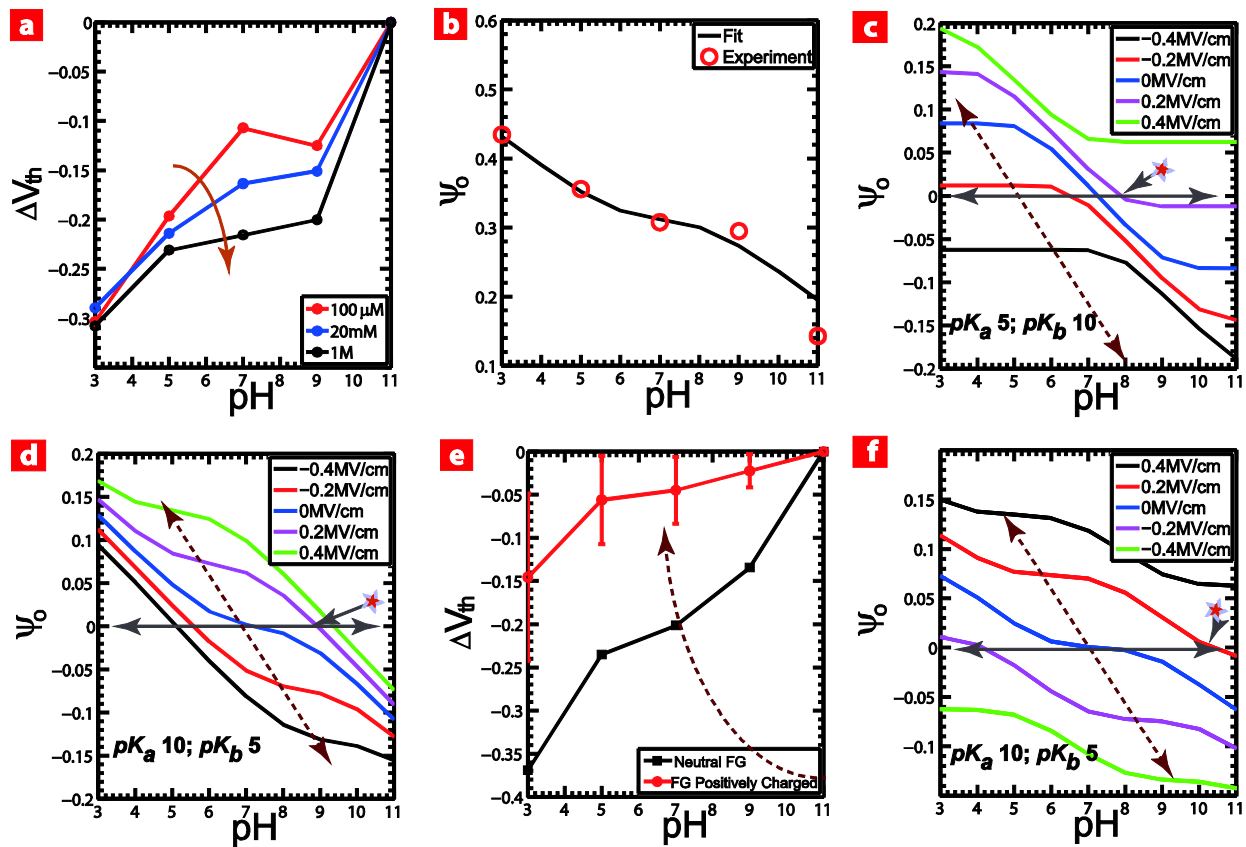


FIG. 5

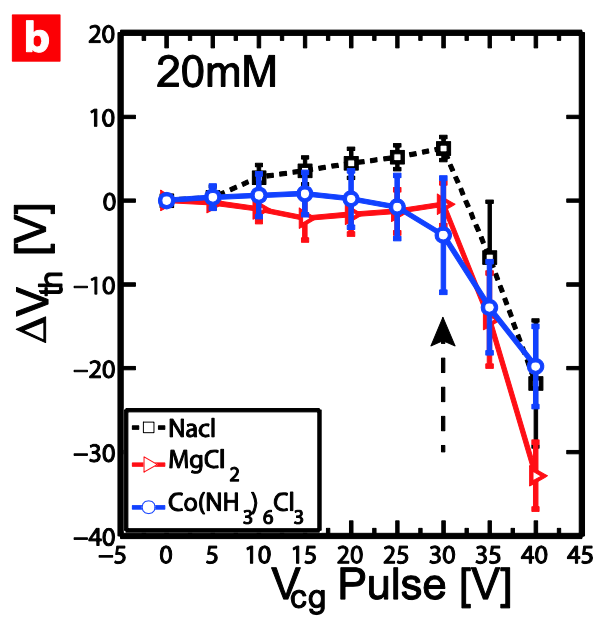
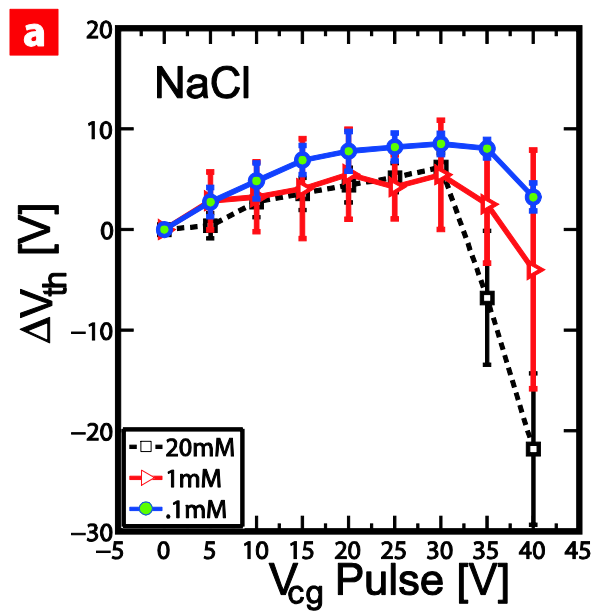


FIG. 6